L. M (leander.michels@ntnu.no), J.O.F (jon.fossum@ntnu.no)

Intercalation and Retention of Carbon Dioxide in a Smectite Clay promoted by Interlayer Cations

L. Michels[1*], J.O. Fossum[1*], Z. Rozynek[1,a], H. Hemmen[1], K. Rustenberg[1], P.A. Sobas[2], G.N. Kalantzopoulos[2], K.D. Knudsen[2,1], M. Janek[3], T.S. Plivelic[4], G.J. da Silva[5].

[1]Department of Physics, Norwegian University of Science and Technology, NTNU. Trondheim, Norway

[2]Physics Department, Institute for Energy Technology, IFE, Kjeller, Norway.

[3]Slovak University of Technology, Bratislava, Slovakia.

[4]MAX IV Laboratory, Lund University, Lund, Sweden.

[5]Instituto de Física, Universidade de Brasília, Brasília, Brasil.

[a]Present address: Institute of Physical Chemistry, Polish Academy of Sciences, Warsaw, Poland.

Abstract: A good material for CO_2 sequestration should possess some specific properties: (i) a large effective surface area with good adsorption capacity, (ii) selectivity for CO_2, (iii) regeneration capacity with minimum energy input, allowing reutilization of the material for CO_2 adsorption, and (iv) low cost and high environmental friendliness. Smectite clays are layered nanoporous materials that may be good candidates in this context. Here we report experiments which show that gaseous CO_2 intercalates into the interlayer nano-space of smectite clay (synthetic fluorohectorite) at conditions close to ambient. The rate of intercalation, as well as the retention ability, of CO_2 and it was found to be strongly dependent on the type of the interlayer cation, which in the present case is Li^+, Na^+ or Ni^{2+}. Interestingly we observe that the smectite Li-fluorohectorite is able to retain CO_2 up to a temperature of 35 °C at ambient pressure, and that the captured CO_2 can be released by heating above this temperature. Our estimations indicate that smectite clays, even with the standard cations analyzed here, capture CO_2 per volume comparable to other materials studied in this context.

Interactions between CO_2 and clay minerals have attracted interest in the scientific community in recent years, partly because geological structures are being investigated as storage sites for anthropogenic CO_2. The cap-rock formations which act as flow barriers and seals in this context are known to contain high proportions of clay minerals[1], and the long-term integrity of these formations is a prerequisite for avoiding CO_2 losses to the atmosphere[2,3]. However, the physical parameters affecting the interactions between CO_2 and clay minerals under reservoir conditions are still not well understood[4].

Clay minerals are materials based on two-dimensional stacks of inorganic layers[5]. In some clay minerals (smectites), non-equivalent substitutions of atoms generate a negative charge on each layer surface which is balanced by exchangeable interlayer cations. These cations are responsible for the differences in the physico-chemical behavior of smectites such as water adsorption and retention, plasticity, swelling etc[6,7]. Smectite clay mineral particles typically consist of up to several hundred layers. Smectites have the ability to intercalate additional molecules into the interlayer space, thereby changing the repetition distance along the layer normal, a process which is known as swelling[8,9]. Intercalation of water can also occurs, since H_2O is a polar molecule, and has been extensively studied with a wide range of techniques, such as neutron[8,10,11] and X-ray scattering[9,12,13], NMR spectroscopy[14-16] tracer experiments[17] or numerical modeling[14,18].

Experiments[19-28] and simulations[18,29-32] have also shown that CO_2 intercalates in some smectite clays, both in supercritical, and in gaseous/liquid form. We have recently demonstrated that CO_2 is able to intercalate in Na-fluorohectorite (NaFh) smectite clay mineral at conditions close to ambient (-20 °C, 5 bar)[22]. These are not the typical conditions found in geological storage sites, but the conditions are relevant if clays are considered as a potential material for the capture or sequestration of CO_2, and also it is of great interest to study CO_2 capture and retention under these conditions for the purpose of understanding the underlying molecular mechanisms. Several porous materials are currently being assessed for the purpose of CO_2 capture and retention[33-35]. In this context, clay-containing materials could have a distinct advantage in that they are both cheap and ubiquitous[31], and also because they generally provide a very large accessible effective surface area that arises from nanolayered stacked structures embedded in a mesoporous powder matrix.

Fluorohectorites (Fh) are synthetic smectites which have been used as a representative and clean model system of natural smectite clays[36]. Synthetic clays have the advantage that they possess a more homogeneous charge distribution, and also contain significantly fewer impurities (e.g. carbonates, (hydr)oxides, silica, and organic matter) than their natural counterparts[37].

In the present work we studied the intercalation of CO_2 in Li-fluorohectorite (LiFh), Na-fluorohectorite (NaFh) and Ni-fluorohectorite (NiFh). The only differences between these samples are the interlayer charge compensating cations used. Intercalation experiments under different temperature and pressure conditions were conducted. In order to investigate the potential of fluorohectorite clays for CO_2 storage and capture, we also quantified the CO_2 adsorption (wt%).

Results

A. CO_2 Intercalation

The layered nature of smectite clays gives rise to well-defined (00l) diffraction peaks, and the angular position of these peaks is a direct measure of the interlayer repetition distance (the d-spacing). Figure 1 displays how the intensity of the (001) diffraction peak grows with time as the samples are exposed to CO_2 at -20 °C and 20 bar. Intercalation of CO_2 in the interlayer space manifests itself as the growth of an intercalation peak at a lower scattering angle than the peak of dry, non-intercalated clay. As the intercalation progresses, the intensity of the CO_2-intercalation peaks increase whereas the scattering from non-intercalated part of the sample decreases and eventually vanishes. LiFh and NaFh show similar intercalation behaviors and the (001) peaks develop at q-values corresponding to d-spacings of 1.196 nm $\left(q = 5.25\ \mathrm{nm}^{-1}\right)$ and 1.240 nm $\left(q = 5.06\ \mathrm{nm}^{-1}\right)$, for LiFh and NaFh respectively. This corresponds to a monolayer of intercalated CO_2. For the NiFh sample we observe a similar intercalation state with d-spacing of 1.219 nm $\left(q = 5.15\ \mathrm{nm}^{-1}\right)$ and in addition the development of another state with a larger d-spacing of 1.311 nm

$\left(q = 4.79\ \mathrm{nm}^{-1}\right)$. To our knowledge, this is the first time such a complex CO_2 intercalation state has been observed in clay mineral.

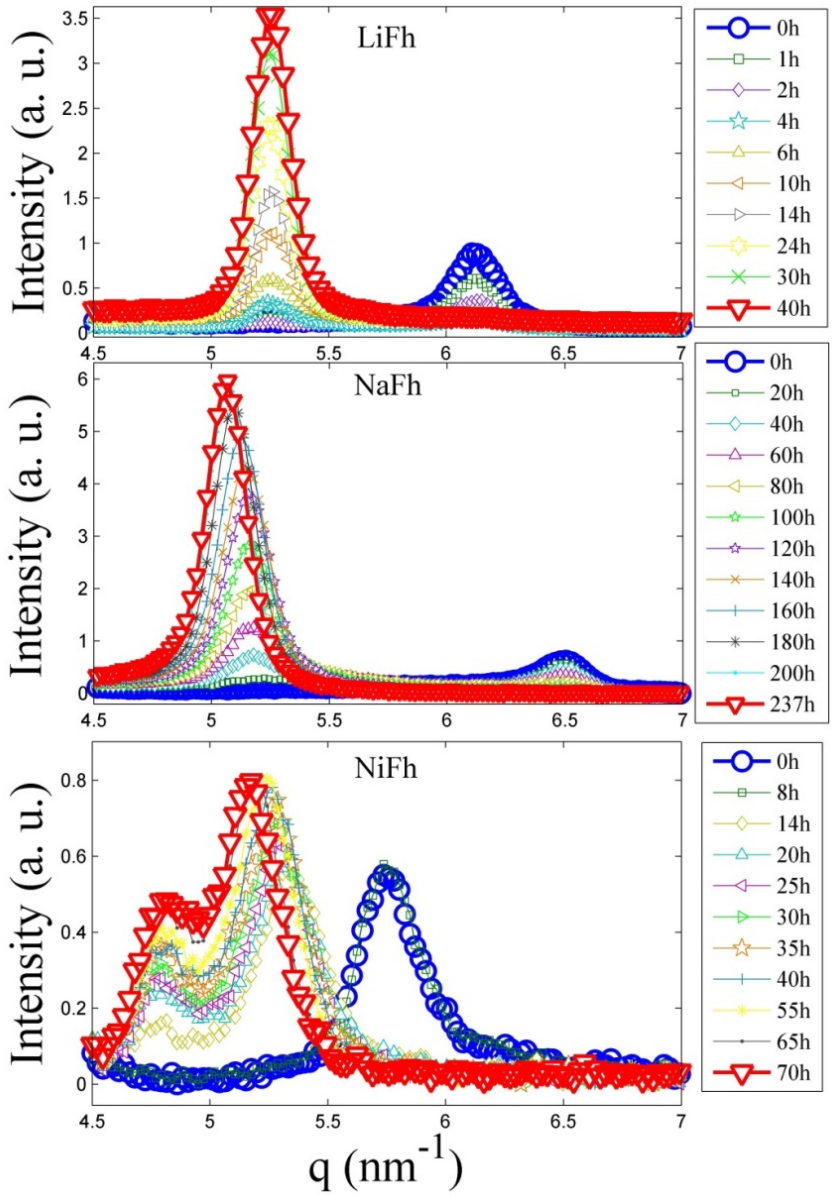

Figure 1: The scattering intensity (arb. units) over a range of q-values at different times (hours), for LiFh, NaFh and NiFh, respectively. In all cases the adsorption conditions were -20 °C and 20 bar. The red line (▽) shows the time at saturation. Experiment performed at NTNU.

Figure 2 shows the comparison of (001) peak intensity vs. time for LiFh, NaFh and NiFh. In this figure the NiFh (001) peak intensities are the one at higher $q \approx 5.2\ \mathrm{nm}^{-1}$, the one at lower $q \approx 4.8\ \mathrm{nm}^{-1}$ and the sum of them, as shown in

figure 1. We observe that the intercalation rate is significantly higher for NiFh and LiFh than for NaFh. This is similar to the case of water intercalation, where cations have been found to determine the stable states at varying relative humidity[18,38-41] as well as the way that clay minerals exfoliate in aqueous dispersion[7,42]. Fripiat et al.[27] suggested that the access of CO_2 molecules to the interlayer space of montmorillonite clay is dependent on the size of the interlayer cation. On the other hand, Giesting et al.[23] studied CO_2-intercalation behavior of K-and Ca-montmorillonite, and also performed repeated measurements under the same conditions, but reported no strong dependence of dynamics on the cations. The dynamics of the CO_2 intercalation can also be followed by observing the disappearance of the scattering intensity of the dehydrated peak, shown in figure S1 in supporting information, which represents the d-spacing in the portion of the sample with no water or CO_2 intercalated.

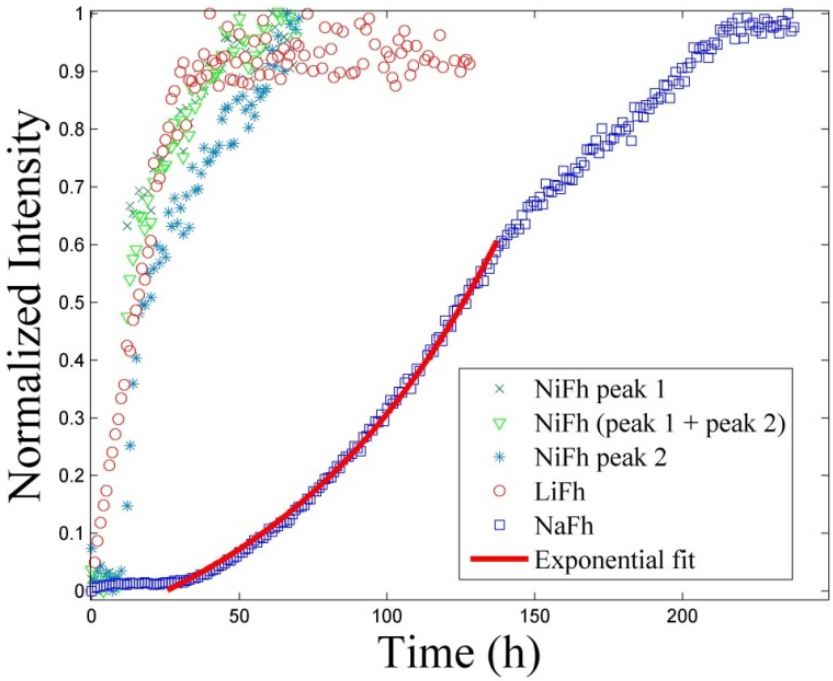

Figure 2: Intensity of the intercalation peak, normalized to the maximum intercalation intensity, as a function of time for different cations at 20 bar and -20 °C. The NiFh diffractogram has two contributions: Peak 1 is the peak with the maximum intensity at highest $q \approx 5.2\ \mathrm{nm}^{-1}$ while peak 2 is the peak with the lowest $q \approx 4.8\ \mathrm{nm}^{-1}$.

A general equation for describing sorption kinetics is[43]:

$$\frac{dn}{dt} = n_0 \frac{1}{\tau} f\left(\frac{n}{n_0}\right) \tag{1}$$

where n is the amount of adsorbed molecules on a surface and $\frac{1}{\tau}$ is a rate constant that depends on temperature and pressure. The equation for the function $f\left(\frac{n}{n_0}\right)$ depends on the type of adsorption mechanism. For a first order adsorption process, i.e. a process where the adsorbed molecules statistically occupies a single adsorption site[44], $f\left(\frac{n}{n_0}\right) = 1 - \frac{n}{n_0}$. In the present case, $\frac{n}{n_0}$ is equal to normalized X-ray intensity (NI), where normalization is performed with respect to the intensity observed at the longest times, where the adsorption capacity of the material is reached. By integrating equation (1), we obtain

$$NI = 1 - \exp\left(-\frac{t}{\tau}\right) \tag{2}$$

which is an exponential growth function towards saturation at 1. Applying the natural logarithm, we have a linear equation with the slope proportional to the rate constant $\frac{1}{\tau}$:

$$-\ln\left(1 - NI\right) = \frac{t}{\tau} \tag{3}$$

The results of plotting the observed normalized intensity in this manner are shown in figure 3. It is evident that equation (3) describes the data for NiFh and LiFh reasonably well, before the full adsorption capacity is reached, i.e. before all the sites have been occupied. However, for NaFh we observe deviation for $-\ln\left(1 - NI\right) < 1.6$,

which we relate to the Na^+ ion providing a stronger layer adherence than the other two ions investigated here, and thus the swelling is more difficult to achieve for the case of Na^+, since the clay layers are closer together in the dehydrated state of NaFh, as shown in figure 1. The difference I q-spacing between the dehydrated and the CO_2 intercalated peak is almost twice for NaFh compared to LiFh and NiFh (figure 1). The dotted horizontal line represents the threshold between two regimes for the case of NaFh: particle swelling plus intercalation of CO_2 (below the line) and intercalation of CO_2 into the swollen interlayer of the clay mineral (above the line). A single exponential growth function $NI = A\exp\left(\frac{t}{\tau_1}\right)$ (shown in figure 2), with $\tau_1 \approx 88$, related to the clay swelling, describes well the data in the initial phase for NaFh, i.e. for $-\ln(1-NI) < 1.6$ in figure 3.

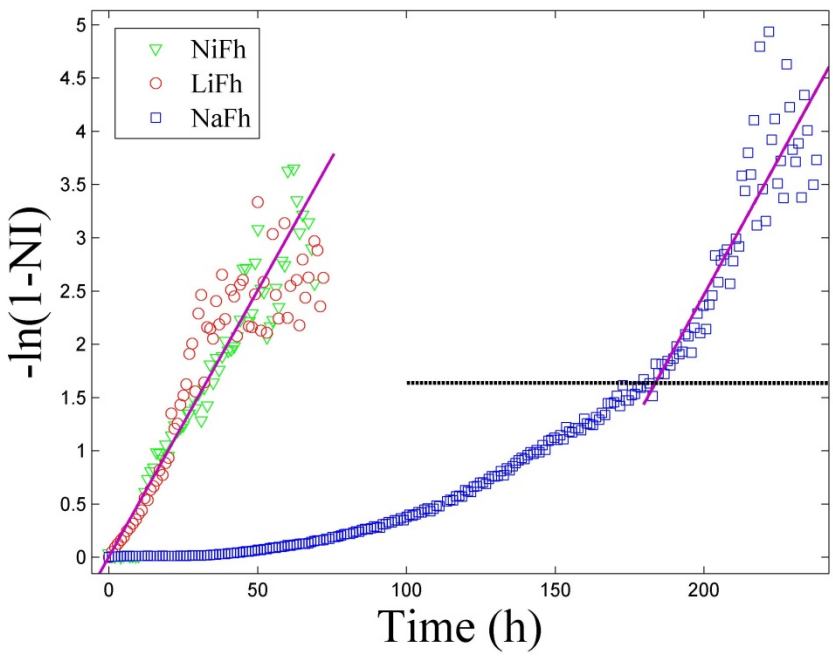

Figure 3: The linearized intensity as function of time. The horizontal dotted line represents the threshold between two regimes for NaFh: Clay swelling accompanied by some intercalation of CO_2 (below the horizontal line), which is described by the exponential function $NI = A\exp\left(\frac{t}{\tau_1}\right)$, and intercalation of CO_2 into the swollen interlayer of the clay mineral (above the horizontal line) described by equations (2) and (3). The initial swelling part of the dynamics is much faster for NiFh and LiFh as compared to NaFh, which is also confirmed in figure S1 in the supporting information.

After the swelling process is finished, which means that the clay does not expand significantly anymore, the intercalation process is cation independent since the slopes of the curves shown in figure 3 are the same for all samples, i.e. $\frac{1}{\tau} = 0.05 \pm 0.005$ hours^{-1}. This corresponds to a time constant τ of approx. 20 hours.

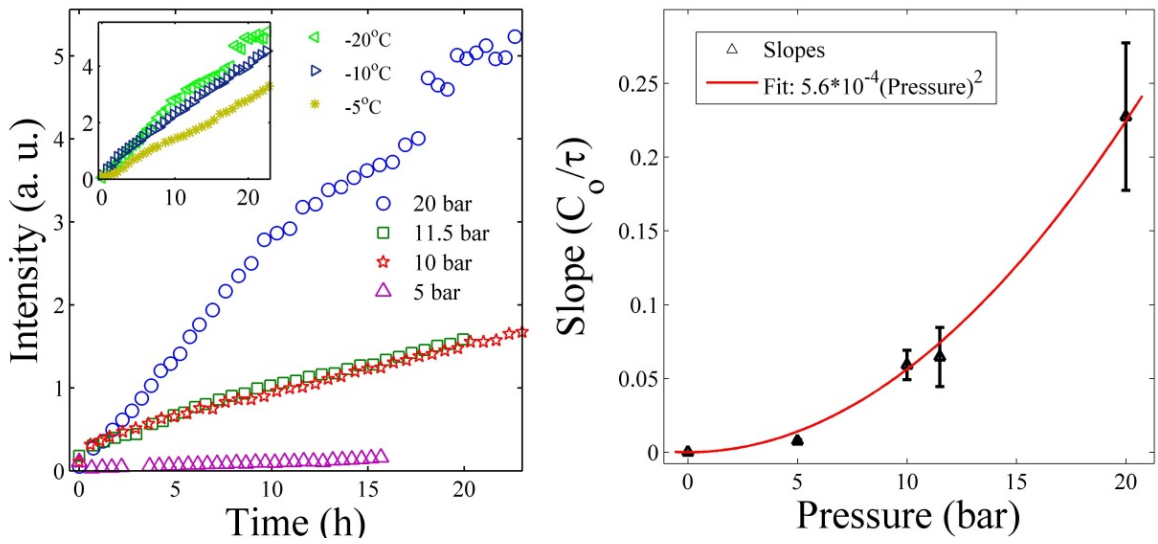

Figure 4: Left panel: The intensity of the (001) CO_2 intercalation peak in LiFh as a function of time for different pressures (at constant temperature of -20 °C). The intercalation rate increases with the pressure. Right panel: The quadratic dependence of the linear fit slopes C_o/τ on CO_2 pressure. Experiment performed at Maxlab.

The dependence of the intercalation intensity at various pressures is shown in figure 4 for LiFh. The results show that the intercalation rate increases with pressure and this observation is in agreement with a previous study of NaFh[22]. We also measured intercalation at various temperatures (at a constant pressure of 20 bar) in the limited temperature range -5, -10 and -20 °C and the data suggests (inset of figure 4) faster adsorption at lower temperature.

The intensity of the CO_2 intercalation peak follows a linear behavior for small times, in agreement with equation (2), which for small times $t << \tau$ becomes $NI \approx \frac{t}{\tau}$. In figure 4 we have not normalized the measured intensities to their saturation at long times, because we did not follow the experiments until saturation, thus the

slopes (S) of the straight lines at short times in figure 4: $S \approx \frac{C_o}{\tau}$ where C_o is a constant. If we assume that the adsorption dynamics after swelling is governed by an average Arrhenius like trapping time, $\tau = \tau_o e^{\frac{E}{k_B T}}$, where, $\frac{1}{\tau_o}$ is an average attempt frequency, E is an average energy barrier, k_B is Boltzmann constant and T is the absolute temperature. Further we can assume that the attempt frequency $\frac{1}{\tau_o}$ increases with pressure, P, i.e. the higher the pressure, the more attempts are made by the CO_2 molecules to cross the adsorption trapping energy barrier E. In right panel of figure 4, we have tested this assumption and fitted an empiric parabolic function to the pressure dependence of $\frac{1}{\tau_o}$. Our temperature measurements are in a such limited range in absolute temperature that they do not allow us to test Arrhenius trapping time assumption, but the desorption data for LiFh (shown below) indicates that the sorption trapping barrier is on the order of magnitude of $\frac{E}{k_B} \approx 300K$. This gives $\tau \approx \tau_o \frac{6\times10^{-4}}{P^2} e^{-\frac{300}{T}}$ where P is in units of bar and T in units of absolute temperature (K). From figure 3 we estimated $\tau \approx 20$ hours for P and T equal to 20 bar and 253 K respectively. This enables us to estimate $\tau_o \approx 5\cdot10^7$ hours, and thus the adsorption time would be $\tau \approx 14$ min for P and T equal to 200 bar and 250 K respectively, if we assume that trapping mechanism for liquid and gas CO_2 are the same.

B. CO_2 retention under ambient conditions

After exposing the three types of clay mineral samples to CO_2 pressure for a sufficiently long time, the CO_2 pressure was released and the cell was continuously flushed with N_2, since it is dry and does not intercalate in the clay minerals, at

atmospheric pressure, while increasing the temperature in steps of 5 °C. A plot of peak intensity versus time at different increasing temperatures is shown in figure 5.

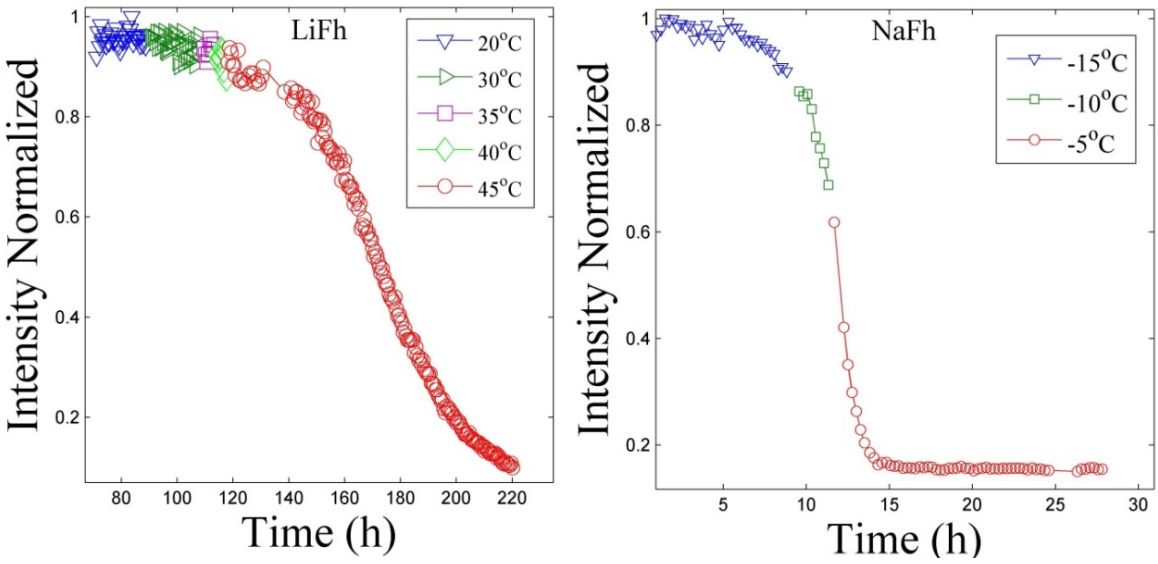

Figure 5: (001) peak intensity of LiFh (left) and NaFh (right) as a function of time for increasing temperatures. Experiments performed at NTNU.

It has previously been concluded that the interlayer CO_2 may cause an irreversible adsorption in clay, i.e. even if a clay sample is not exposed to the CO_2 gas, CO_2 molecules remain in the interlayer space[45,46]. This means that once intercalated with CO_2 the clay mineral will retain these molecules. However, a temperature change can affect the CO_2 retention[47,48] and this makes the process of intercalation and release truly reversible. We found that at a certain threshold temperature, the intensity decreases until the contribution to the scattered intensity from the clay mineral with intercalated CO_2 is negligible. Simultaneously, the peak corresponding to the dehydrated LiFh and NaFh reappears (data not shown). The threshold temperature, at which the CO_2 is desorbed from the interlayer space of the clays, is highly dependent on the type of interlayer cation used. For LiFh, this temperature is about 35 ^{o}C, whereas for NaFh it is about -15 °C (figure 5). This is consistent with the difference in size between the smaller Li^+ cation versus the larger Na^+ cation. Li^+ has a more concentrated charge distribution than Na^+ and can thus polarize the CO_2 molecule

more, forming a stronger bond to it. In the case of NiFh the release, like the intercalation, has more complex features, as shown in figure 6.

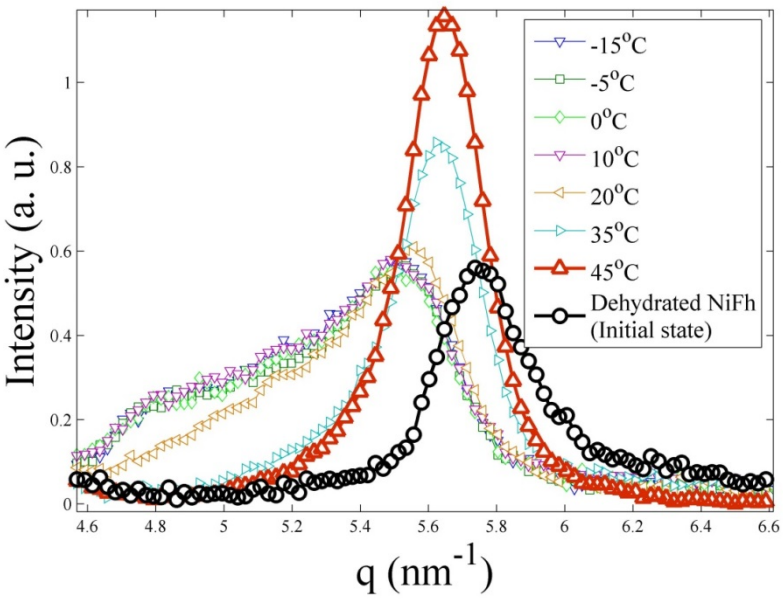

Figure 6: (001) peak intensity of NiFh as a function of the scattering vector q for different temperatures in N_2 at atmospheric pressure. As a reference the initial dehydrated peak of NiFh is included in the graph (circles, which is the same as the 0h curve in figure 1). Experiments performed at NTNU.

Comparing NiFh spectrum in figure 1 with figure 6 one can see that upon heating the second CO_2 peak merges with the first CO_2 peak for NiFh. With increasing temperature, the intensity of the peak at lowest q value (about 4.8 nm^{-1}) decreases and at 45 °C, it completely disappears while the highest q value peak shifts to higher values and eventually contains all the (001) scattering. It appears that the final intercalation state is different from the original dehydrated state. This could suggest the formation of a complex CO_2-Ni^{2+} structure within the interlayer space of the NiFh clay mineral, not present in the case of LiFh and NaFh.

C. Pressure composition Temperature Experiments

Figure 7 shows the excess CO_2 adsorption isotherm of LiFh, obtained with the pcT-setup, described in the methods section. The excess adsorption is the amount of material taken up by the sample. The adsorption measurements were performed at room temperature and pressure range from 1 bar up to 45 bar. The initial part of the

isotherm (0 to ca. 9 bar) represents diffusion of CO_2 into the mesoporous network[49] of the clay powder. Above approximately 9 bar it is likely that the swelling process of the clay has nearly finished, and this will result in increased intercalation kinetics. With further increase in CO_2 pressure, the excess of CO_2 is seen to rise up to around 11 wt. % at a pressure of about 38 bar. At higher pressures, the apparent amount of adsorbed CO_2 starts to decrease, likely due to the formation of an adsorbed layer with higher density and comparable to the volume of the clay mineral, associated with approach to the critical pressure for CO_2[50,51].

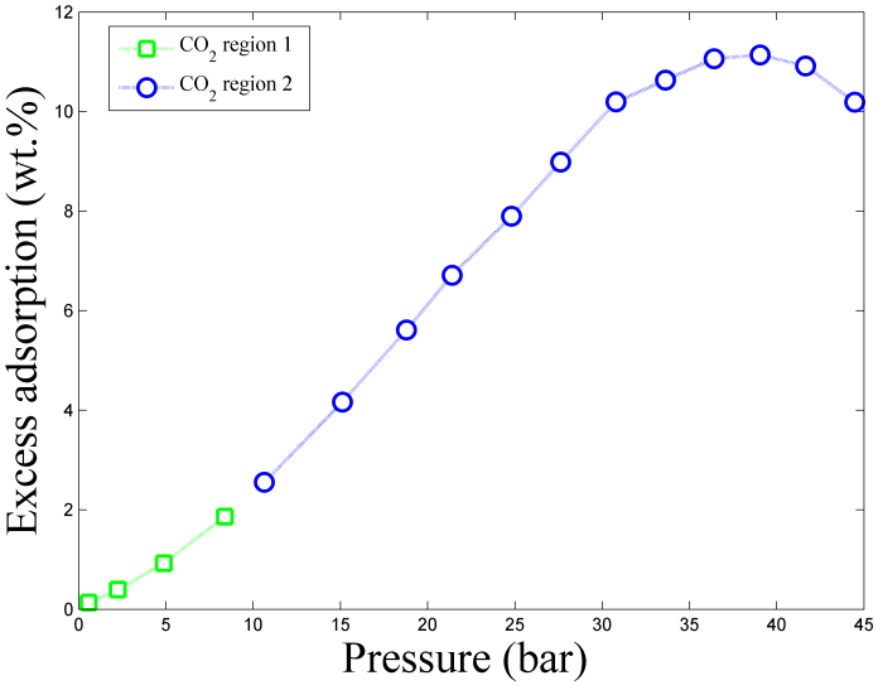

Figure 7: Excess CO_2 adsorption isotherm of Li-fluorohectorite at room temperature and pressure range 0 to 45 bar. The region 1 (squares) describes diffusion of CO_2 into the clay mineral powder mesoporous network, and subsequent intercalation within the region 2 (circles). Experiment performed at IFE.

Discussion

The uptake of CO_2 per weight of clay mineral can be inferred if it is assumed that the number of CO_2 molecules coordinating exchangeable cations is similar to the number of H_2O molecules within the interlayer space for the corresponding H_2O-clay

system (at monohydrated state). This is approximately 2.4 molecules for each interlayer cation[16,15]. In case of LiFh and NaFh these would result in:

$$\frac{m_{\mathrm{CO_2}}}{m_{\mathrm{NaFh}}} \approx \frac{m_{\mathrm{CO_2}}}{m_{\mathrm{LiFh}}} \approx 14\% \tag{3}$$

which is the same order of magnitude as measured by pcT (Figure 6), in this pressure range. This gives an amount of 3.2 mmols of CO_2/g of LiFh, and makes the clay minerals an interesting candidate for anthropogenic CO_2 storage. For other good CO2 capturing materials this number vary from 6.00 mmol of CO_2/g, for e.g. metal organic frameworks (MOFs)[52], to 5.00 mmol of CO_2/g for Zeolites[53]. Both numbers are higher than the one we find for the clay mineral fluorohectorite. However, if we compare the adsorbed mmol of CO_2 per volume of the material, rather than mmol of CO_2 per adsorbent mass, considering that the densities of zeolites (~2.2 g/cm^3) and MOFs (~2.0 g/cm^3) are lower than that of the clay minerals (~2.8 g/cm^3). We find that a clay mineral, even with the cations considered here, is able to capture nearly the same mass of CO_2 per volume (0.23 ton of CO_2 per m^3 of sample) as compared to the "best" zeolites (0.29 ton of CO_2 per m^3 of sample), or MOFs (0.32 ton of CO_2 per m^3 of sample) in this context. These numbers were calculated assuming 60% of packing density for all the materials. The commonly used benchmark Zeolite 13X captures 0.14 ton of CO_2 per m^3 of sample.

Methods

X-ray diffraction measurements were primarily performed on an in-house (NTNU, Trondheim) Bruker NanoSTAR X-ray scattering instrument, attached to a Xenox stationary electron impact source with a copper anode, producing Kα-radiation. The scattered intensity was recorded by a two-dimensional multiwire grid Xe gas detector (HI-STAR, Bruker). The beam diameter of the setup is 400 μm and the detectable range of momentum transfer q is $(2.5 < q < 7.5)$ nm^{-1} (q is defined here as $q = 4\pi \sin\theta / \lambda$, where θ is the scattering angle and λ the wavelength of the X-

rays). Complementary X-ray scattering data were collected at the I911-4 beamline of MAX IV laboratory using a 2D CCD detector (165 mm diameter, from Marresearch, GmbH) and 0.91 Å wavelengths.

The samples were mounted in a custom-made sample holder[22] which allows temperature control in the range of -30 °C to 45 °C and pressures in the range from ambient to 20 bar. To allow X-rays to pass through the sample, the cell has Kapton windows on both sides of the sample volume. Internal channels connect gas from valves on the surface of the cell to the sample volume, and the gas pressure is controlled by standard reduction valves. The sample cell is depicted in figure S2 in the supporting information.

In both X-ray setups, two-dimensional diffractograms were recorded and then azimuthally averaged to produce plots of intensity versus scattering vector, I vs q. Data reduction consisted in subtracting a background and normalizing the intensity profiles to the peak produced by the Kapton windows (see Hemmen et al.[22] for details). The intensity, position and width of the intercalation peaks were found by fitting the peaks to Pseudo-Voigt profiles[54,55].

The LiFh clay mineral used in the experiments was purchased from Corning Inc. (with nominal chemical formula: $M_x\left(Mg_{6-x}Li_x\right)Si_8O_{20}F_4$ per unit cell[56], where M is the interlayer cation (Li^+, Na^+ and Ni^{2+}) and x the amount which balances the charge of clay mineral layers (x = 1.2 for monovalent ions, and x = 0.6 for divalent ions). Each sample consisted of 7 ± 1 mg of clay powder packed in the available space in the sample chamber. Typically such packed clay powder samples have a mesoporosity of about 40%[49], which in the present case enables access of the employed gases to the layered nanoporous structures that make up the individual powder grains.

At ambient conditions, these clay mineral samples are in the monohydrated state[9,57]. Since the uptake of the CO_2 molecules may be affected by the initial H_2O concentration[58], we investigated dehydrated native samples. For dehydration, the

samples were heated in an oven at 125 °C for more than three hours. To remove residual humidity from the cell after loading the clay, and to ensure that the sample remained dry, the cell was flushed with N_2-gas. An X-ray scan was also recorded at ambient temperature and pressure while flushing with N_2 to confirm that the sample remained dehydrated before starting the CO_2 intercalation experiments. The sample was subsequently cooled to -15 °C temperature before the gas was changed to CO_2. The gas outlet of the cell was closed and the pressure increased.

The CO_2 used for experiments has a purity of 99.999% (Yara Praxair, grade 5). The N_2 gas has a purity of 99.9999% (Yara Praxair, grade 6). To obtain a satisfactory signal-to-noise ratio, we varied the acquisition times from 30 to 60 minutes, depending on CO_2 pressure, due to differences in X-ray absorption.

Pressure-composition-Temperature (pcT) isotherms were measured in a calibrated in-house built (IFE, Kjeller) volumetric Sieverts-type apparatus in order to obtain information on CO_2 adsorption. Approximately 300 mg of Li-fluorohectorite was inserted in a sample holder and was degassed at 115 °C under dynamic vacuum (<10 mbar), overnight, to remove residual humidity. Adsorption isotherms were acquired in the 0 – 45 bar range, with 3 bar step between each aliquot measurement at room temperature. The CO_2 adsorption data were baseline corrected by the adsorption data collected from N_2.

References

1 Cole, D. R., Chialvo, A. A., Rother, G., Vlcek, L. & Cummings, P. T. Supercritical fluid behavior at nanoscale interfaces: Implications for CO2 sequestration in geologic formations. *Philosophical Magazine* **90**, 2339-2363, doi:10.1080/14786430903559458 (2010).

2 Hildenbrand, A., Schlomer, S. & Krooss, B. M. Gas breakthrough experiments on fine-grained sedimentary rocks. *Geofluids* **2**, 3-23, doi:10.1046/j.1468-8123.2002.00031.x (2002).

3 Wollenweber, J. *et al.* Experimental investigation of the CO2 sealing efficiency of caprocks. *International Journal of Greenhouse Gas Control* **4**, 231-241, doi:10.1016/j.ijggc.2010.01.003 (2010).

4 de Jong, S. M., Spiers, C. J. & Busch, A. Development of swelling strain in smectite clays through exposure to carbon dioxide. *International Journal of Greenhouse Gas Control* **24**, 149-161, doi:10.1016/j.ijggc.2014.03.010 (2014).

5 Boulet, P., Greenwell, H. C., Stackhouse, S. & Coveney, P. V. Recent advances in understanding the structure and reactivity of clays using electronic structure calculations. *Journal of Molecular Structure-Theochem* **762**, 33-48, doi:10.1016/j.theochem.2005.10.028 (2006).

6 F. Bergaya, G. L. *Handbook of Clay Science*. 1 edn, Vol. 1 (Elsevier Science, 2006).

7 Hansen, E. L. *et al.* Swelling transition of a clay induced by heating. *Scientific Reports* **2**, doi:10.1038/srep00618 (2012).

8 Bordallo, H. N. *et al.* Quasi-elastic neutron scattering studies on clay interlayer-space highlighting the effect of the cation in confined water dynamics. *Journal of Physical Chemistry C* **112**, 13982-13991, doi:10.1021/jp803274j (2008).

9 da Silva, G. J., Fossum, J. O., DiMasi, E., Maloy, K. J. & Lutnaes, S. B. Synchrotron x-ray scattering studies of water intercalation in a layered synthetic silicate. *Physical Review E* **66**, doi:10.1103/PhysRevE.66.011303 (2002).

10 Malikova, N. *et al.* Water diffusion in a synthetic hectorite clay studied by quasi-elastic neutron scattering. *Journal of Physical Chemistry C* **111**, 17603-17611, doi:10.1021/jp0748009 (2007).

11 Jimenez-Ruiz, M., Ferrage, E., Delville, A. & Michot, L. J. Anisotropy on the Collective Dynamics of Water Confined in Swelling Clay Minerals. *Journal of Physical Chemistry A* **116**, 2379-2387, doi:10.1021/jp201543t (2012).

12 da Silva, G. J., Fossum, J. O., DiMasi, E. & Maloy, K. J. Hydration transitions in a nanolayered synthetic silicate: A synchrotron x-ray scattering study. *Physical Review B* **67**, doi:10.1103/PhysRevB.67.094114 (2003).

13 Dazas, B. *et al.* Smectite fluorination and its impact on interlayer water content and structure: A way to fine tune the hydrophilicity of clay surfaces? *Microporous and Mesoporous Materials* **181**, 233-247, doi:10.1016/j.micromeso.2013.07.032 (2013).

14 Porion, P., Michot, L. J., Faugere, A. M. & Delville, A. Structural and dynamical properties of the water molecules confined in dense clay sediments: A study combining H-2 NMR spectroscopy and multiscale numerical modeling. *Journal of Physical Chemistry C* **111**, 5441-5453, doi:10.1021/jp067907p (2007).

15 Tenorio, R. P., Engelsberg, M., Fossum, J. O. & da Silva, G. J. Intercalated Water in Synthetic Fluorhectorite Clay. *Langmuir* **26**, 9703-9709, doi:10.1021/la100377s (2010).

16 Tenorio, R. P., Alme, L. R., Engelsberg, M., Fossum, J. O. & Hallwass, F. Geometry and dynamics of intercalated water in Na-fluorhectorite clay hydrates. *Journal of Physical Chemistry C* **112**, 575-580, doi:10.1021/jp0766407 (2008).

17 Jansson, M. & Eriksen, T. E. In situ anion diffusion experiments using radiotracers. *Journal of Contaminant Hydrology* **68**, 183-192, doi:10.1016/s0169-7722(03)00149-9 (2004).

18 Tambach, T. J., Hensen, E. J. M. & Smit, B. Molecular simulations of swelling clay minerals. *Journal of Physical Chemistry B* **108**, 7586-7596, doi:10.1021/jp049799h (2004).

19 Schaef, H. T. *et al.* In situ XRD study of Ca2+ saturated montmorillonite (STX-1) exposed to anhydrous and wet supercritical carbon dioxide. *International Journal of Greenhouse Gas Control* **6**, 220-229, doi:10.1016/j.ijggc.2011.11.001 (2012).

20 Loring, J. S. *et al.* In Situ Molecular Spectroscopic Evidence for CO2 Intercalation into Montmorillonite in Supercritical Carbon Dioxide. *Langmuir* **28**, 7125-7128, doi:10.1021/la301136w (2012).

21 Ilton, E. S., Schaef, H. T., Qafoku, O., Rosso, K. M. & Felmy, A. R. In Situ X-ray Diffraction Study of Na+ Saturated Montmorillonite Exposed to Variably Wet Super Critical CO2. *Environmental Science & Technology* **46**, 4241-4248, doi:10.1021/es300234v (2012).

22 Hemmen, H. *et al.* X-ray Studies of Carbon Dioxide Intercalation in Na-Fluorohectorite Clay at Near-Ambient Conditions. *Langmuir* **28**, 1678-1682, doi:10.1021/la204164q (2012).

23 Giesting, P., Guggenheim, S., van Groos, A. F. K. & Busch, A. X-ray Diffraction Study of K- and Ca-Exchanged Montmorillonites in CO2 Atmospheres. *Environmental Science & Technology* **46**, 5623-5630, doi:10.1021/es3005865 (2012).

24 Giesting, P., Guggenheim, S., van Groos, A. F. K. & Busch, A. Interaction of carbon dioxide with Na-exchanged montmorillonite at pressures to 640 bars: Implications for CO2 sequestration. *International Journal of Greenhouse Gas Control* **8**, 73-81, doi:10.1016/j.ijggc.2012.01.011 (2012).

25 Busch, A. *et al.* Carbon dioxide storage potential of shales. *International Journal of Greenhouse Gas Control* **2**, 297-308, doi:10.1016/j.ijggc.2008.03.003 (2008).

26 Sozzani, P. *et al.* Nanoporosity of an organo-clay shown by hyperpolarized xenon and 2D NMR spectroscopy. *Chemical Communications*, 1921-1923, doi:10.1039/b602040b (2006).

27 Fripiat, J. J., Cruz, M. I., Bohor, B. F. & Thomas, J. Interlamellar Adsorption of Carbon-Dioxide by Smectites. *Clays and Clay Minerals* **22**, 23-30, doi:10.1346/ccmn.1974.0220105 (1974).

28 Thomas, J. & Bohor, B. F. Surface Area of Montmorillonite from Dynamic Sorption of Nitrogen and Carbon Dioxide. *Clays and Clay Minerals* **16**, 83-&, doi:10.1346/ccmn.1968.0160110 (1968).

29 Krishnan, M., Saharay, M. & Kirkpatrick, R. J. Molecular Dynamics Modeling of CO2 and Poly(ethylene glycol) in Montmorillonite: The Structure of Clay-Polymer Composites and the Incorporation of CO2. *Journal of Physical Chemistry C* **117**, 20592-20609, doi:10.1021/jp405321t (2013).

30 Yang, N. & Yang, X. Molecular simulation of swelling and structure for Na-Wyoming montmorillonite in supercritical CO2. *Molecular Simulation* **37**, 1063-1070, doi:10.1080/08927022.2010.547939 (2011).

31 Randall T. Cygan, V. N. R. a. E. M. M. Natural Materials for Carbon Capture. Report No. SAND2010-7217, (Sandia National Laboratories, Albuquerque, New Mexico, 2010).

32 Botan, A., Rotenberg, B., Marry, V., Turq, P. & Noetinger, B. Carbon Dioxide in Montmorillonite Clay Hydrates: Thermodynamics, Structure, and Transport from Molecular Simulation. *Journal of Physical Chemistry C* **114**, 14962-14969, doi:10.1021/jp1043305 (2010).

33 Yang, S. *et al.* A partially interpenetrated metal-organic framework for selective hysteretic sorption of carbon dioxide. *Nature Materials* **11**, 710-716, doi:10.1038/nmat3343 (2012).

34 Vaidhyanathan, R. *et al.* Direct Observation and Quantification of CO2 Binding Within an Amine-Functionalized Nanoporous Solid. *Science* **330**, 650-653, doi:10.1126/science.1194237 (2010).

35 Banerjee, R. *et al.* High-throughput synthesis of zeolitic imidazolate frameworks and application to CO2 capture. *Science* **319**, 939-943, doi:10.1126/science.1152516 (2008).

36 Hemmen, H., Alme, L. R., Fossum, J. O. & Meheust, Y. X-ray studies of interlayer water absorption and mesoporous water transport in a weakly hydrated clay. *Physical Review E* **82**, doi:10.1103/PhysRevE.82.036315 (2010).

37 Bergaya, F. & Lagaly, G. in *Developments in Clay Science* Vol. Volume 5 (eds Bergaya Faïza & Lagaly Gerhard) 213-221 (Elsevier, 2013).

38 Malikova, N., Dubois, E., Marry, V., Rotenberg, B. & Turq, P. Dynamics in Clays - Combining Neutron Scattering and Microscopic Simulation. *Zeitschrift Fur Physikalische Chemie-International Journal of Research in Physical Chemistry & Chemical Physics* **224**, 153-181, doi:10.1524/zpch.2010.6097 (2010).

39 Gates, W. P. *et al.* Neutron Time-of-Flight Quantification of Water Desorption Isotherms of Montmorillonite. *Journal of Physical Chemistry C* **116**, 5558-5570, doi:10.1021/jp2072815 (2012).

40 Tamura, K., Yamada, H. & Nakazawa, H. Stepwise hydration of high-quality synthetic smectite with various cations. *Clays and Clay Minerals* **48**, 400-404, doi:10.1346/ccmn.2000.0480311 (2000).

41 Ferrage, E., Lanson, B., Michot, L. J. & Robert, J.-L. Hydration Properties and Interlayer Organization of Water and Ions in Synthetic Na-Smectite with Tetrahedral Layer Charge. Part 1. Results from X-ray Diffraction Profile Modeling. *Journal of Physical Chemistry C* **114**, 4515-4526, doi:10.1021/jp909860p (2010).

42 Skipper, N. T., Smalley, M. V., Williams, G. D., Soper, A. K. & Thompson, C. H. Direct Measument of the Electric Double-Layer Structure in Hydrated Lithium Vermiculite Clays by Neutron-Difraction. *Journal of Physical Chemistry* **99**, 14201-14204, doi:10.1021/j100039a003 (1995).

43 Gasparini, E. *et al.* Thermal dehydroxylation of kaolinite under isothermal conditions. *Applied Clay Science* **80-81**, 417-425, doi:10.1016/j.clay.2013.07.017 (2013).

44 Liu, Y. & Shen, L. From Langmuir Kinetics to First- and Second-Order Rate Equations for Adsorption. *Langmuir* **24**, 11625-11630, doi:10.1021/la801839b (2008).

45 Romanov, V. N. Evidence of irreversible CO2 intercalation in montmorillonite. *International Journal of Greenhouse Gas Control* **14**, 220-226, doi:10.1016/j.ijggc.2013.01.022 (2013).
46 Cygan, R. T., Romanov, V. N. & Myshakin, E. M. Molecular Simulation of Carbon Dioxide Capture by Montmorillonite Using an Accurate and Flexible Force Field. *Journal of Physical Chemistry C* **116**, 13079-13091, doi:10.1021/jp3007574 (2012).
47 Azzouz, A. *et al.* Truly reversible capture of CO2 by montmorillonite intercalated with soya oil-derived polyglycerols. *International Journal of Greenhouse Gas Control* **17**, 140-147, doi:10.1016/j.ijggc.2013.04.013 (2013).
48 Azzouz, A. *et al.* Polyol-modified layered double hydroxides with attenuated basicity for a truly reversible capture of CO2. *Adsorption-Journal of the International Adsorption Society* **19**, 909-918, doi:10.1007/s10450-013-9498-3 (2013).
49 Knudsen, K. D., Fossum, J. O., Helgesen, G. & Bergaplass, V. Pore characteristics and water absorption in a synthetic smectite clay. *Journal of Applied Crystallography* **36**, 587-591, doi:10.1107/s0021889803001778 (2003).
50 Schaef, H. T. *et al.* Surface Condensation of CO2 onto Kaolinite. *Environmental Science & Technology Letters* **1**, 142-145, doi:10.1021/ez400169b (2013).
51 Melnichenko, Y. B., Wignall, G. D., Cole, D. R. & Frielinghaus, H. Adsorption of supercritical CO2 in aerogels as studied by small-angle neutron scattering and neutron transmission techniques. *Journal of Chemical Physics* **124**, doi:10.1063/1.2202324 (2006).
52 An, J. & Rosi, N. L. Tuning MOF CO2 Adsorption Properties via Cation Exchange. *Journal of the American Chemical Society* **132**, 5578-+, doi:10.1021/ja1012992 (2010).
53 Walton, K. S., Abney, M. B. & LeVan, M. D. CO2 adsorption in Y and X zeolites modified by alkali metal cation exchange. *Microporous and Mesoporous Materials* **91**, 78-84, doi:10.1016/j.micromeso.2005.11.023 (2006).
54 Wertheim, G. K., Butler, M. A., West, K. W. & Buchanan, D. N. Determination of Gaussian and Lorentzian Content of Experimental Line-Shapes. *Review of Scientific Instruments* **45**, 1369-1371, doi:10.1063/1.1686503 (1974).
55 Cox, D. E., Toby, B. H. & Eddy, M. M. Acquisition of Powder Diffraction Data with Synchrotron Radiation. *Australian Journal of Physics* **41**, 117-131 (1988).
56 Kaviratna, P. D., Pinnavaia, T. J. & Schroeder, P. A. Dielectric properties of smectite clays. *Journal of Physics and Chemistry of Solids* **57**, 1897-1906, doi:10.1016/s0022-3697(96)00076-5 (1996).
57 Michels, L. *et al.* EXAFS and XRD studies in synthetic Ni-fluorohectorite. *Applied Clay Science* **96**, 60-66, doi:10.1016/j.clay.2014.04.031 (2014).
58 Loring, J. S. *et al.* In Situ Study of CO2 and H2O Partitioning between Na-Montmorillonite and Variably Wet Supercritical Carbon Dioxide. *Langmuir* **30**, 6120-6128, doi:10.1021/la500682t (2014).

Acknowledgments

L.M, J.O.F, Z.R, P.S, and K.D.K acknowledge the CLIMIT Program of the Research Council of Norway (Project number 200041). MAX IV laboratory is acknowledged for providing the beamtime at I911-4 under the proposal 20110154. The authors acknowledge Geir Helgesen for discussions and Ole Tore Buset for technical assistance.

Author contribution statement

J.O.F and K. D. K. planned the experiments. H.H., K.R. and L.M. designed the sample cell used for the X-ray experiments. L.M., Z.R. and G.J. da S. performed the X-ray experiments at NTNU. H.H., K.R., J.O.F. and T. S. P. performed the synchrotron experiments at Maxlab. P.A.S., G.N.K. and K.D.K. performed the pcT experiments and the associated data analysis. L.M., M.J. and G.J. da S. did the main part of the X-ray

data analysis. L.M. and J.O.F. wrote the discussion of the results and also the manuscript, and all authors revised the manuscript before submission.